AGU PUBLICATIONS

JGR

Journal of Geophysical Research: Atmospheres

RESEARCH ARTICLE
10.1002/2017JD027969

Special Section:
Deep Convective Clouds and Chemistry 2012 Studies (DC3)

Modeling the TTL at Continental Scale for a Wet Season: An Evaluation of the BRAMS Mesoscale Model Using TRO-Pico Campaign, and Measurements From Airborne and Spaceborne Sensors

Abhinna K. Behera[1], Emmanuel D. Rivière[1], Virginie Marécal[2], Jean-François Rysman[3], Claud Chantal[3], Geneviève Sèze[4], Nadir Amarouche[5], Mélanie Ghysels[1], Sergey M. Khaykin[6], Jean-Pierre Pommereau[6], Gerhard Held[7,8], Jérémie Burgalat[1], and Georges Durry[1]

[1]GSMA, UMR CNRS 7331, UFR Sciences Exactes et Naturelles, Reims, France, [2]CNRM, UMR3589, Météo-France, CNRS, Toulouse, France, [3]LMD/IPSL, CNRS UMR 8539, École Polytechnique, Université Paris Saclay, ENS, PSL Research University, Sorbonne Universités, UPMC Université Paris 06, CNRS, Palaiseau, France, [4]LMD, IPSL, UPMC, CNRS, École Polytechnique, ENS, Paris, France, [5]Division technique de l'INSU, Place Aristide Briand, Meudon, France, [6]LATMOS/IPSL, UVSQ Université Paris-Saclay, UPMC University Paris 06, CNRS, Guyancourt, France, [7]Instituto de Pesquisas Meteorológicas, Universidade Estadual Paulista, Bauru, Brazil, [8]Retired since 2014,

Key Points:
- The model depicts the typical variability of temperature and water vapor in the tropical tropopause layer, and the gravity wave properties
- High modeled cloud tops are observed at the overshooting locations detected by MHS, showing similar variability as GOES-12 measurements
- Impact of stratospheric sudden warming occurring in the Arctic is detected in the tropical tropopause layer over South America

Supporting Information:
- Supporting Information S1
- Text S1
- Figure S1
- Figure S2
- Figure S3

Correspondence to:
A. K. Behera,
abhinna-kumar.behera@univ-reims.fr

Citation:
Behera, A. K., Rivière, E. D., Marécal, V., Rysman, J.-F., Chantal, C., Sèze, G., et al. (2018). Modeling the TTL at continental scale for a wet season: An evaluation of the BRAMS mesoscale model using TRO-Pico campaign, and measurements from airborne and spaceborne sensors. *Journal of Geophysical Research: Atmospheres*, *123*. https://doi.org/10.1002/2017JD027969

Received 27 OCT 2017
Accepted 7 FEB 2018
Accepted article online 13 FEB 2018

Abstract In order to better understand the water vapor (WV) intrusion into the tropical stratosphere, a mesoscale simulation of the tropical tropopause layer using the BRAMS (Brazilian version of Regional Atmospheric Modeling System (RAMS)) model is evaluated for a wet season. This simulation with a horizontal grid point resolution of 20 km × 20 km cannot resolve the stratospheric overshooting convection (SOC). Its ability to reproduce other key parameters playing a role in the stratospheric WV abundance is investigated using the balloon-borne TRO-Pico campaign measurements, the upper-air soundings over Brazil, and the satellite observations by Aura Microwave Limb Sounder, Microwave Humidity Sounder, and Geostationary Operational Environmental Satellite 12. The BRAMS exhibits a good ability in simulating temperature, cold-point, WV variability around the tropopause. However, the simulation is typically observed to be warmer by ∼2.0°C and wetter by ∼0.4 ppmv at the hygropause, which can be partly affiliated with the grid boundary nudging of the model by European Centre for Medium-Range Weather Forecasts operational analyses. The modeled cloud tops show a good correlation (maximum cross-correlation of ∼0.7) with Geostationary Operational Environmental Satellite 12. Furthermore, the overshooting cells detected by Microwave Humidity Sounder are observed at the locations, where 75% of the modeled cloud tops are higher than 11 km. Finally, the modeled inertia-gravity wave periodicity and wavelength are comparable with those deduced from the radio sounding measurements during TRO-Pico campaign. The good behavior of BRAMS confirms the SOC contribution in the WV abundance, and variability is of lesser importance than the large-scale processes. This simulation can be used as a reference run for upscaling the impact of SOC at a continental scale for future studies.

1. Introduction

The presence of water vapor (WV) in the stratosphere is now recognized to play a role in the surface climate (Avery et al., 2017; Dessler et al., 2013; Forster & Shine, 1999; Solomon et al., 2010). H_2O is also a key species for stratospheric chemistry, especially for the ozone layer (Graf et al., 1998; Solomon, 1988). Itnot only enhances the abundance of OH^- radical which controls the lifetime of many other chemical species in the stratosphere but it also modifies the processes linked with O_3 depletion (Shindell, 2001; Solomon, 1999). The radiative and microphysical feedbacks of H_2O abundance in the stratosphere may also govern the formation of polar stratospheric clouds over the Arctic or the Antarctic, as the stratosphere cools down (Ramaswamy et al., 1996; Toon et al., 1989).

The seminal work of Brewer (1949) puts to the fore the mechanisms linked with the abundance of stratospheric WV. It is mainly modulated by the intrusions through the tropical tropopause layer (TTL) (Highwood & Hoskins, 1998). This layer extends from the mean convective outflow (∼14 km or 150 hPa) to the highest

altitude reached by severe deep convection (~19 km or 70 hPa) above which the mass flux is constant (Fueglistaler et al., 2009). That depicts a smooth transition from a convectively modulated troposphere to a radiatively modulated stratosphere at the tropics (Gettelman & de F Forster, 2002; Seidel et al., 2001). Many field campaign measurements (e.g., Jensen, Thornberry, et al., 2017) and modeling studies (e.g., Smalley et al., 2017) report that it is the region of complex dynamical interactions at different scales and speeds, where most of them have a potential role in the stratospheric WV budget. These complex dynamical activities can be resolved into processes such as the slow ascent due to the positive net radiative heating above 14 km to 15 km (e.g., Gettelman et al., 2004; Küpper et al., 2004), the deep convection penetrating through the lapse rate tropopause (e.g., Corti et al., 2008; Danielsen, 1982; Khaykin et al., 2009; Romps & Kuang, 2009), and the atmospheric waves generated by deep convection (e.g., Dinh et al., 2016; Schoeberl et al., 2015). Understanding all these processes and their interactions is of prime importance, given the potential role of the TTL's WV abundance in the climate evolution (Dessler et al., 2016; Randel & Jensen, 2013).

Several trajectory studies driven by meteorological analyses succeed at least qualitatively in reproducing the WV abundance and its variability rather well in the TTL (e.g., Dessler et al., 2014; Schoeberl et al., 2012) without considering the severe overshooting convection exceeding the level of neutral buoyancy, hereafter referred to as convective overshooting (COV). Thus, it is deduced that most of the WV entry to the stratosphere is due to an advection-condensation mechanism during the slow ascent toward the very cold tropopause, followed by the sedimentation of ice particles (Holton & Gettelman, 2001; Liu, Fueglistaler, & Haynes, 2010). This freezing-drying or cold-trap mechanism leads to the dehydration of air mass entering into the stratosphere at the tropics, and particularly very efficient in the Pacific Ocean where the cold-point tropopause (CPT) is the coldest (Hasebe et al., 2007; Schoeberl & Dessler, 2011). As such, the tropical CPT, a stratospheric feature having dependency on the chemistry of O_3, CO_2, and H_2O (Kirk-Davidoff et al., 1999) and deep convection (Kuang & Bretherton, 2004), regulates H_2O abundance in the lower stratosphere (Randel et al., 2006; Wang et al., 2015).

Gravity waves play a key role in the stratosphere-troposphere exchange (Fritts & Alexander, 2003; Holton et al., 1995). They have a well-observed influence on the net radiative heating and WV exchange that occurs in the upper troposphere-lower stratosphere (UTLS) (Holton, 1983) and are also known for its energy dissipation that can cool down the ambient atmosphere—increasing the favorable conditions for the formation of ice clouds in the TTL (Kim et al., 2016). Admittedly, the deep convection in the tropics is a major driving force in producing inertia-gravity waves (Alexander et al., 1995; Jewtoukoff et al., 2013). Recent works of Schoeberl et al. (2015, 2016) and Kim & Alexander (2013, 2015) put to the fore its significance in the modulation of ice particle formation and WV abundance in the TTL.

In contrast to these large-scale processes, COV may penetrate into the stratosphere, hereafter denoted as stratospheric overshooting convection (SOC), injecting ice particles into an environment that is often subsaturated, leading to the sublimation of ice in the stratosphere and an increase of WV. This is concluded both by in situ observations (e.g., Khaykin et al., 2009, 2016; Schiller et al., 2009) and modeling studies at the convective system scale (e.g., Chaboureau et al., 2007; Chemel et al., 2009; Liu, Rivière, et al., 2010). The signature of individual overshooting turrets cannot be identified through the satellite-borne WV measurements at global scale, because either of the coarse vertical resolution (e.g., MLS) or the poor precision (e.g., Atmospheric Infrared Sounder) to detect local WV enhancement within a narrow range of altitude in the TTL. Consequently, the quantitative role of SOC on the stratospheric WV with respect to the large-scale dehydration has not been estimated directly so far. However, the stratospheric WV enhancement due to a single event has been estimated to range between 100 t (Hassim & Lane, 2010), 300 t to 500 t (Liu, Rivière, et al., 2010), and 2776 t (Dauhut et al., 2015) with a frequency estimation of 13 overshooting events per minute in the tropical belt (Iwasaki et al., 2010). Lelieveld et al. (2007) estimate the annual mean of upward H_2O flux ~600t min^{-1} across 75 hPa on the tropical belt from the general circulation model ECHAM5/MESSy1 during the halogen occultation experiment. Ueyama et al. (2015) estimate an enhancement of ~0.3 ppmv of H_2O across 100 hPa at a large-scale in the Southern Hemisphere from the trajectory study initiated from convective cloud tops. An indirect signature of the SOC at global scale can be obtained by studying the diurnal cycle of MLS H_2O mixing ratio due to deep convection reaching higher than 100 hPa (Carminati et al., 2014), highlighting the regions where convection is most active, and confirming former results of Liu and Zipser (2005). But none of these aforementioned studies are able to quantify the impact of SOC in the global abundance of stratospheric WV.

One method to advance our knowledge in this topic is the 3-D modeling approach. Because overshooting turrets are known to be of very limited area (typically of a few km^2 horizontally), the cloud resolving model resolution must be of 1 km or less horizontally and of a few hectometers vertically to properly resolve this process. This makes it difficult to compute a global impact of the SOC on the stratospheric WV abundance. The current work proposes a possible strategy to upscale its effect in a global model, or, as a first step, in a regional model at a continental scale by the use of a subgrid-scale nudging of hydration (or dehydration). A priori, a detailed evaluation of a model should be performed disclosing the key parameters linked to WV abundance in the TTL, that is, height and position of deep convection, thermal structure of the TTL, and inertia-gravity waves generated by convection. This is the aim of the present paper. To set up this platform, we use the Brazilian Regional Atmospheric Modeling System (BRAMS), a 3-D mesoscale model to simulate the TTL over a large part of Brazil during a particular wet season from November 2012 to March 2013. Furthermore, we also take advantage of the balloon-borne measurements from the TRO-Pico campaign at Bauru (22.31°S, 49.05°W) during the same 5 months of observation period (FMOP), radio soundings (RS) at different locations in Brazil, and spaceborne measurements like the Geostationary Operational Environmental Satellite (GOES-12), Microwave Limb Sounder (MLS), and Microwave Humidity Sounder (MHS), in order to evaluate our proposal.

The paper is organized as follows: section 2 describes the mesoscale model, as well as the strategy of its evaluation. Subsequently, section 3 provides the details of the validation tools used, section 4 evaluates the modeled thermal structure and WV variability against the TRO-Pico measurements, section 5 evaluates the simulated deep convection against GOES-12 and MHS, and section 6 discusses the ability of BRAMS in reproducing the inertia-gravity wave. A summary, including further objectives, is given in section 7.

2. Methodology

2.1. Model Description and Setup

The BRAMS (version 4.2 with meteorology tailored to tropics (Freitas et al., 2009)) is a limited area weather model developed at Centro de Previsão de Tempo e Estudos Climáticos/Instituto Nacional de Pesquisas Espaciais, which is derived from the RAMS: version 5.04 (Cotton et al., 2003; Pielke et al., 1992) of the University of Colorado/ATMET. It incorporates a double-moment microphysical scheme having seven hydrometeors (liquid cloud droplets and rain for liquid particles; pristine, snow, hail, graupel, and aggregates for ice particles) (Meyers et al., 1997). Here the number concentrations and mass mixing ratios of hydrometeors are prognostic variables of BRAMS, assuming that each hydrometeor size follows a gamma function $\Gamma(\nu)$ distribution, ν being the shape parameter. The main differences between BRAMS and RAMS are the parameterization of subgrid-scale cumulus convection, the surface scheme, and the soil moisture initialization. BRAMS incorporates the Grell parameterization of deep convection (Grell & Dévényi, 2002).

On the research and application side, Marécal et al. (2007) show that the BRAMS model is able to simulate the WV distribution in the TTL, but on a relatively shorter time scale using a coarser vertical grid point resolution. Our approach is almost the same, as such a horizontal grid point resolution of 20 km × 20 km is used, keeping in mind the spatial and temporal scale of simulation and computing cost. This resolution is too coarse to produce SOC, which should occur typically on a 1 km × 1 km grid point resolution given a convective parameterization scheme in the model. For initialization and the 6-hourly nudging at the grid boundary of the simulation, the ECMWF (European Centre for Medium-Range Weather Forecasts) operational analyses in pressure levels are incorporated, with no nudging inside the domain. The simulation is carried out for the FMOP having 105 vertical levels starting from surface to 30 km altitude with a resolution of ∼100 m between 14.5 km and 18.3 km. The domain of simulation covers the latitude from 7.28°S to 28.41°S and longitude from 38.42°W to 61.48°W, which encompasses a large part of the tropical region of Brazil (the domain of simulation is shown in Figure 5). Note that an evaluation of another mesoscale model WRF (Weather Research and Forecasting) in the TTL has been performed already by Evan et al. (2013), but with a coarser horizontal and vertical grid point resolution on a larger domain. While BRAMS and WRF have a similar origin (Skamarock et al., 2005), the version 4.2 offers a lower number of options due to its optimized aspects for the tropical meteorology. However, a comparison between BRAMS and WRF would be a subjective paper itself, but the following features are highlighted: Data assimilation: in case of BRAMS-only nudging prevails, while WRF includes a more sophisticated var-assimilation system; dynamical core: nonhydrostatic model with possibility of hydrostatic model; boundary condition: a sponge layer at the top of the domain, possibly cyclic conditions at the lateral boundaries with boundary conditions from meteorological operational analysis; double-moment

microphysical scheme: seven types of hydrometeors (five for ice) in BRAMS (Meyers et al., 1997), while five types of hydrometeors (three for ice) in WRF (Morrison et al., 2009).

For our study, the subgrid-scale parameterization for deep convection with the ensemble closure type is chosen. This closure is shown to be the best for tracer transport by deep convection over the Maritime continent (Arteta et al., 2009). The CO_2 vertical profiles in the SiB submodel (Sellers, Randall, et al., 1996; Sellers, Tucker, et al., 1996) initialization and in the radiative parameterization scheme (Harrington, 1997) are updated to 395 ppmv from the values of Pico-SDLA CO_2 spectrometer of the TRO-Pico campaign. For the bulk microphysics, the shape parameter ν is set to 2.1 for each category of hydrometeor after performing sensitivity tests in order to get the optimal results based on the comparisons with satellite observations (tests are made using ν = 1.9, 2.0, and 2.1). A 5 km deep sponge layer is used to damp the gravity waves at the top of the domain. The typical time step of integration is ~10 s to 30 s to maintain the simulation stability.

2.2. Strategy of Model Evaluation

We utilize the TRO-Pico campaign measurements to validate the modeled parameters, that is, temperature, H_2O mixing ratio, and inertia-gravity waves. TRO-Pico is a French funded project which aims at studying the TTL's WV budget at a local scale, but on two different time scales: the full wet season corresponding roughly to a FMOP from November 2012 to March 2013 and the most active convective periods (IOP, intensive observation period) during the FMOP. The most active convective periods of sampling (IOP) correspond to March 2012 (IOP1) and January–February 2013 (IOP2). During the IOPs, a set of light instruments were launched under small balloons (500 m^3 to 1500 m^3 open balloons or 1.2 kg meteorological rubber balloons) as close as possible to convective events. The measured parameters were H_2O, CH_4, CO_2 mixing ratios, and particles/aerosols concentration or backscattering ratio. In this study, we make use of the H_2O mixing ratio from the Pico-SDLA and the FLASH-B stratospheric hygrometers during the IOP2, from the Pico-SDLA during the FMOP (see Figure 3a for the list of the profiles), and from the MLS: version 4.2 measurements (see section 4). We also make use of temperature (see section 4) and wind (see section 6) measurements from RS92 SGP radiosondes of the TRO-Pico campaign, and some more temperature measurements from the RS over Brazil during the FMOP. A detailed description of TRO-Pico can be found in Ghysels et al. (2016). Thereafter, the performance of the model in producing convective clouds, both in spatial and temporal precision is investigated, using GOES-12 and MHS measurements (see section 5).

3. Validation Tools

3.1. RS92

Within the TRO-Pico campaign, RS with Vaisala RS92 SGP PTU are used. The temperature uncertainty in RS92 is 0.5°C, while the pressure uncertainties provided by the manufacturer for two different pressure ranges are 1.5 hPa for 1,080 hPa to 100 hPa, and 0.6 hPa for 100 hPa to 3 hPa. The RS92 were launched from 23 January to 12 February 2013, with a frequency of one to four measurements per day. Concurrently, zonal wind (u) and meridional wind (v) are collected for inertia-gravity wave analysis. Furthermore, temperature and pressure measurements from the RS92 on board the FLASH-B payload are also taken into account in the temperature climatology (see section 4).

3.2. Upper-Air Soundings

During the FMOP, regular balloon-borne RS measurements of temperature are retrieved from the upper-air sounding database of Wyoming University for six stations in Brazil (see Figure 5d), viz., Alta Floresta (SBAT: 9.86°S, 56.10°W), Curitiba (SBCT: 25.51°S, 49.16°W), Foz do Iguaçu (SBFI: 25.51°S, 54.58°W), Brasilia (SBBR: 15.85°S, 47.93°W), Couiabá (SBCY: 15.65°S, 56.10°W), and Galeão/Rio de Janeiro (SBGL: 22.81°S, 43.25°W).

3.3. Pico-SDLA

Pico-SDLA hygrometer is a compact, lightweight, direct absorption infrared spectrometer. The hygrometer allows probing WV at 2.63 μm over a 1 m optical path length in ambient air. The measurement principle is simple: H_2O mixing ratio is extracted from the absorbed signal applying the Beer-Lambert law, knowing temperature and pressure. A full description of the instrument, including its uncertainties, is provided by Ghysels et al. (2016). In the TRO-Pico flight conditions, the measurement uncertainty for a unitary spectrum (10 ms acquisition time, not averaged) in the TTL ranges from 3.5% to 7.5%. In extreme conditions at the CPT (measured to be −85.0°C), the uncertainty was estimated to be 4.4%. The precision can be improved by averaging over N unitary spectra, enhancing the signal-to-noise ratio by a factor of $\sqrt{N}$. The time schedule

of the different measurements used in this study can be found in Ghysels et al. (2016) (see also Figure 3a). Most of the observations were made during the IOP2, while eight other profiles were taken from the FMOP.

3.4. FLASH-B

FLASH is a Lyman-alpha hygrometer. The balloon version of FLASH (FLASH-B) is a compact lightweight sonde developed at the Central Aerology Observatory Russia for balloon-borne WV measurements in the upper troposphere and the stratosphere (Yushkov et al., 1998). The instrument is based on the fluorescent method (Bertaux & Delannoy, 1978), which uses the photodissociation of H_2O molecules exposed to ultraviolet radiation ($\lambda < 137$ nm) in vacuum followed by the measurement of fluorescence of excited OH^- radicals using a photomultiplier in photon-counting mode. The intensity of the fluorescent light sensed by the photomultiplier is directly proportional to the H_2O mixing ratio under stratospheric conditions (150 hPa to 10 hPa). Each FLASH-B instrument is calibrated in the laboratory against a reference dew point hygrometer MBW 373L (Vömel et al., 2007). The detection limit for a 4 s integration time at stratospheric conditions is approximately 0.1 ppmv, while accuracy is limited by the calibration error amounting to a relative uncertainty of 4%. The typical measurement precision in the stratosphere is 5% to 6%, whereas the combined relative uncertainty in WV concentration is less than 10% throughout the stratosphere.

Here we apply a composite data set of WV profiles from both Pico-SDLA and FLASH-B hygrometers to evaluate the modeled TTL. Ghysels et al. (2016) have shown a relative difference of H_2O mixing ratio <1.9% between Pico-SDLA and FLASH-B in the TTL, based on a couple of coincident flights during the TRO-Pico campaign. This constitutes one of the best intercomparison results of WV sensors, making it a fully consistent data set.

3.5. MLS

Satellite-borne aura MLS (version 4.2) WV measurements are used for the FMOP around Bauru, that is, a domain of 24.00°S to 19.00°S and 55.50°W to 43.50°W. As Aura is a Sun-synchronous satellite, depending on the local time and pressure level, MLS H_2O measurement precision can vary in the UTLS, and is more reliable at monthly and seasonal time scales. Version 4.2 of H_2O measurement tends to possess dry biases of >20% at the tropopause level. A full technical description of the MLS: version 4.2 can be found in Livesey et al. (2015) and Yan et al. (2016).

3.6. GOES-12

In order to assess the simulated convective cloud cells in intensity, temporal and spatial precision over Brazil during the FMOP, cloud products (Derrien & Gléau, 2005; Sèze et al., 2015) obtained from the radiance data of visible and infrared radiometer on board GOES-12 provided by the SAFNWC (Satellite Application Facility for supporting NoWCasting and very short range forecasting) are used. In this data set, the cloud top height is available every 15 min with a spatial resolution of 4 km × 4 km. In the SAFNWC scheme, after separating the cirrus clouds from the high opaque clouds using a multispectral threshold test, the cloud radiative altitude of optically thick high cloud is obtained from the 10.8 μm brightness temperature (T_B), ancillary temperature, and humidity profiles. This radiative cloud altitude is placed at 0.4 km to 1.6 km below the physical boundaries of the cloud depending on the opacity of cloud top (Garnier et al., 2012; Minnis et al., 2008). For high-level thin clouds, a correction for semitransparency is applied using two infrared channels, a window channel and a sounding one (Menzel et al., 1983; Schmetz et al., 1993).

3.7. MHS

The locations of COV, that is, the convective turrets penetrating to the TTL, which may also enter into the stratosphere (SOC), within the domain of simulation for the FMOP are collected from the MHS on board the National Oceanic and Atmospheric Administration and Meteorological Operational polar orbiting satellites. We probe the modeled cloud tops to investigate whether the BRAMS is able to produce very high clouds at the locations where overshooting cells (>14 km) were detected. This examination is important for further application of BRAMS to study the impact of SOC on the TTL at a large scale.

This verification is made by using a climatology based on a satellite-borne microwave radiometer, following a method developed by and assessed in Hong et al. (2005) and Rysman et al. (2017). Specifically, they take advantage of the sensitivity of WV channels to frozen hydrometeors for detecting atmospheric convection, and to discriminate COV from the deep convection. This method has been previously used in the tropics by Hong et al. (2008), in Brazil by Funatsu et al. (2012), and in the Mediterranean by Rysman et al. (2016). Using a microwave radiometer and an X-band radar on board a scientific aircraft, Hong et al. (2005) state that for clear-sky conditions, the T_B measured by the three WV channels is always higher for channels with frequencies

farther away from the central frequency, but within convective clouds this relationship is observed to be reversed. Based on these properties, a criterion is deduced for detecting COV using the difference of T_B between the WV channels. The present study uses the climatology of COV derived from MHS by Rysman et al. (2017).

4. Evaluation of the TTL Temperature and WV

4.1. Temperature Evolution

4.1.1. Bauru: TRO-Pico Campaign

Figure 1 shows the time evolution of the vertical structure of the TTL temperature profile from 23 January to 12 February 2013 radiosonde ascents with RS92, BRAMS, and ECMWF operational analyses, respectively, at Bauru. Data availability of RS92 is shown using the (black) cross marks, and missing points are linearly interpolated. It should be noted that RS92 provides only 1 to 4 measurements per day, whereas BRAMS has 24 (hourly) data points per day, and ECMWF operational analyses has 4 regular data points throughout the observation period (IOP2).

In Figure 1a, the RS92 measurements show a succession of mild and very cold periods in the first part of IOP2 in the TTL. The cold periods are characterized by temperatures below −85.0°C around the cold-point (27 and 29 January and "2 February"—the coldest one being −87.7°C, marked with a white box in the plot). The second part of the IOP2 is significantly warmer, especially around 6–8 February 2013. It can be noted that the coldest periods correspond to the CPT having the highest altitudes which are typically above 80 hPa. Conversely, the warmer periods are associated with CPT below 100 hPa. Figure 1b shows the corresponding simulated version of temperature series. It follows the same structure of the observed time evolution, with a strong cooling of the TTL at the end of January/beginning of February, followed by a warming around 6–8 February, and a slight cooling at the end of the IOP2. The CPT series is very similar to the measured one of RS92. The coldest CPT is observed on 29 January 2013 (−84.8°C marked with the white box), the same coldest period as per RS92 measurement (2 February 2013), but a bit warmer and appearing few days earlier to the observation. The difference between the observation and the modeled temperature is higher than the RS92 precision of 0.5°C. It can also be noticed that the magnitude of the cooling in the model is not as high as the observations.

In order to examine whether the cooling and warming tendencies, apparent both in the model and in the RS92 measurements, are due to large-scale advection of cold air in the TTL or not, the temperature series from the ECMWF operational analyses used for the boundary conditions of the BRAMS simulation are also displayed in Figure 1c at a position (22.00°S, 49.00°W) near to Bauru, recalling that the ECMWF analyses are nudged just at the boundaries, not at the center of the domain of simulation. It shows that the temperature field follows a similar time evolution, as observed in the RS92 and the simulation (Figures 1a and 1b), respectively. Furthermore, the coldest CPT falls in the same period (−83.7°C marked with the white box)—end of January/beginning of February—and is a bit warmer and higher in comparison to RS92. Since we are using the pressure levels to extract the ECWMF operational analyses (in the UTLS, they correspond to 150 hPa, 100 hPa, 70 hPa, 50 hPa, and 30 hPa), the CPT is poorly resolved compared to the ones in BRAMS or in RS92, yet they do display the warming of CPT at the end of January/beginning of February 2013. It can be deduced that most of the time evolution shown here is the consequence of a large-scale process rather than due to the severe convection, which cannot be resolved in the ECMWF analyses. An anomalously cold UTLS is confirmed to be related with the stratospheric sudden warming (SSW) in the Arctic with a consequently large-scale cooling in the tropical belt observed during January and February 2013 in the ATTREX campaign (Evan et al., 2015), also concluded in section S1 in the supporting information. Further comments on this event can be found in section 4.2.

4.1.2. Other Locations in South America: Probing Into CPT

Figure 2 calls attention to the variability of the altitude and temperature series of CPT retrieved from the upper-air database with the concurrent modeled CPT. The altitude time series of the CPT simulated by the BRAMS show a similar pattern of time evolution as observed in RS measurements, although they seem to be warmer and lower in altitude. A summary of biases among them (Table 1) are expressed in two ways. First, they are calculated as the standard deviation (σ) of the differences (δ) for each individual data point between RS versus BRAMS. Second, they are given by $\bar{X}_{\mathrm{BRAMS}} - \bar{X}_{\mathrm{RS}}$, where $\bar{X}$ denotes the mean value of the CPT during the observation period.

Table 1 quantifies the findings from Figure 2, where the results from BRAMS are always warmer than the observations. This warm bias is higher than the 0.5°C precision of the RS92.

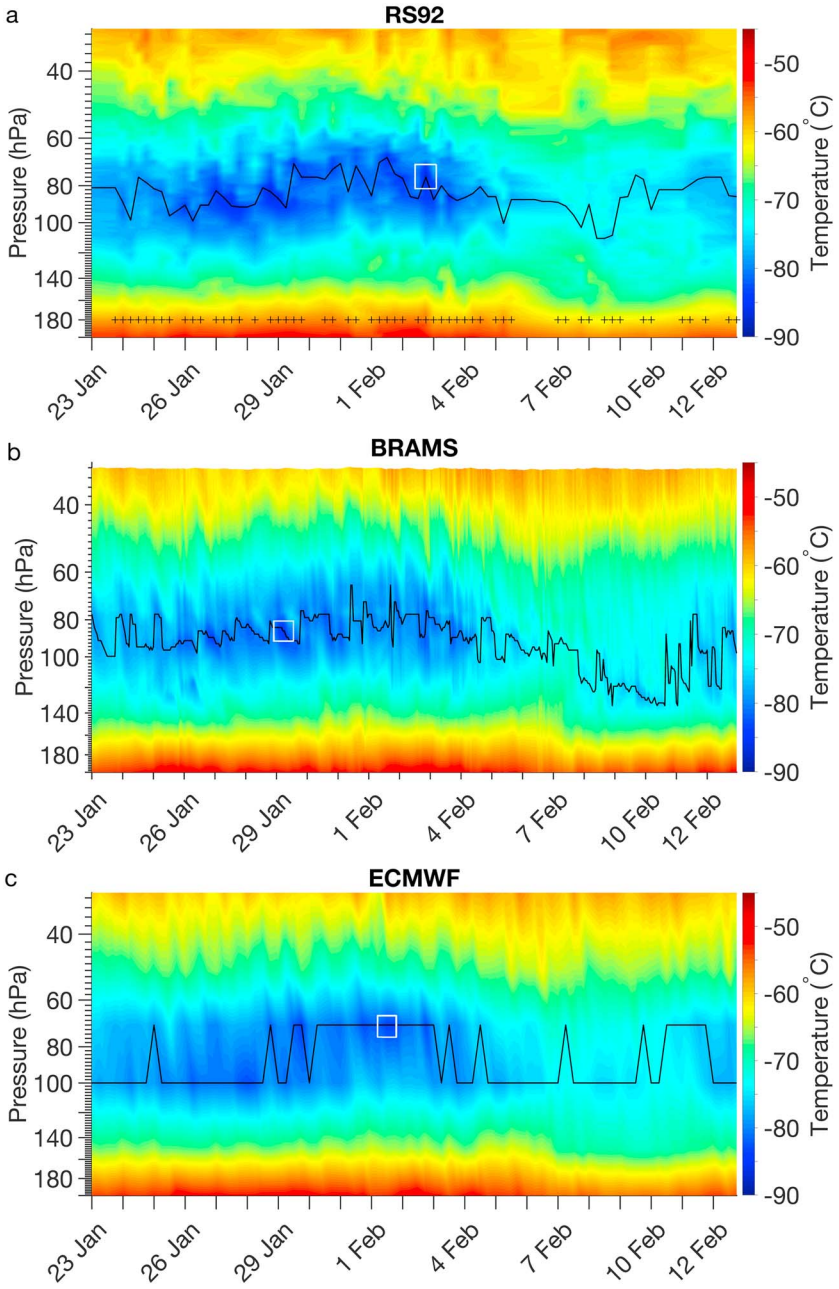

Figure 1. (a) Temperature profile from radio soundings (RS92 SGP), obtained at Bauru (22.31°S, 49.05°W) during the intensive observation period 2 of the TRO-Pico campaign. The time of each sounding is indicated by plus symbols. The black line represents the cold-point tropopause (CPT) altitude. The white box shows the coldest CPT, viz., ~ −88°C observed at ~70 hPa on 2 February 2013. (b) Concurrent temperature profile from the Brazilian version of Regional Atmospheric Modeling System (BRAMS) analyses at the same location, based on hourly data. The white box corresponds to the coldest CPT, viz., ~ −85°C observed at ~85 hPa on 29 January 2013. (c) Concurrent temperature profile near Bauru from the European Centre for Medium-Range Weather Forecasts (ECMWF) analyses, based on four data points per day. The white box corresponds to the coldest CPT, viz., ~ −84°C observed at ~70 hPa on 1 February 2013.

This can be explained by two facts: first, the vertical grid point resolution of ~100 m near the TTL is typically coarser by a factor of about 3 than the RS vertical resolution (~35 m). Second, the ECMWF operational analyses data used for nudging the initial and boundary conditions of BRAMS grid points are already coarser and warmer. Therefore, BRAMS should be qualitatively warmer and lower in representing the CPT. A third hypothesis could be proposed here; that is, the 20 km horizontal grid point resolution implies that COV and SOC cannot be resolved explicitly by the model; thus, the associated cooling of the TTL is absent.

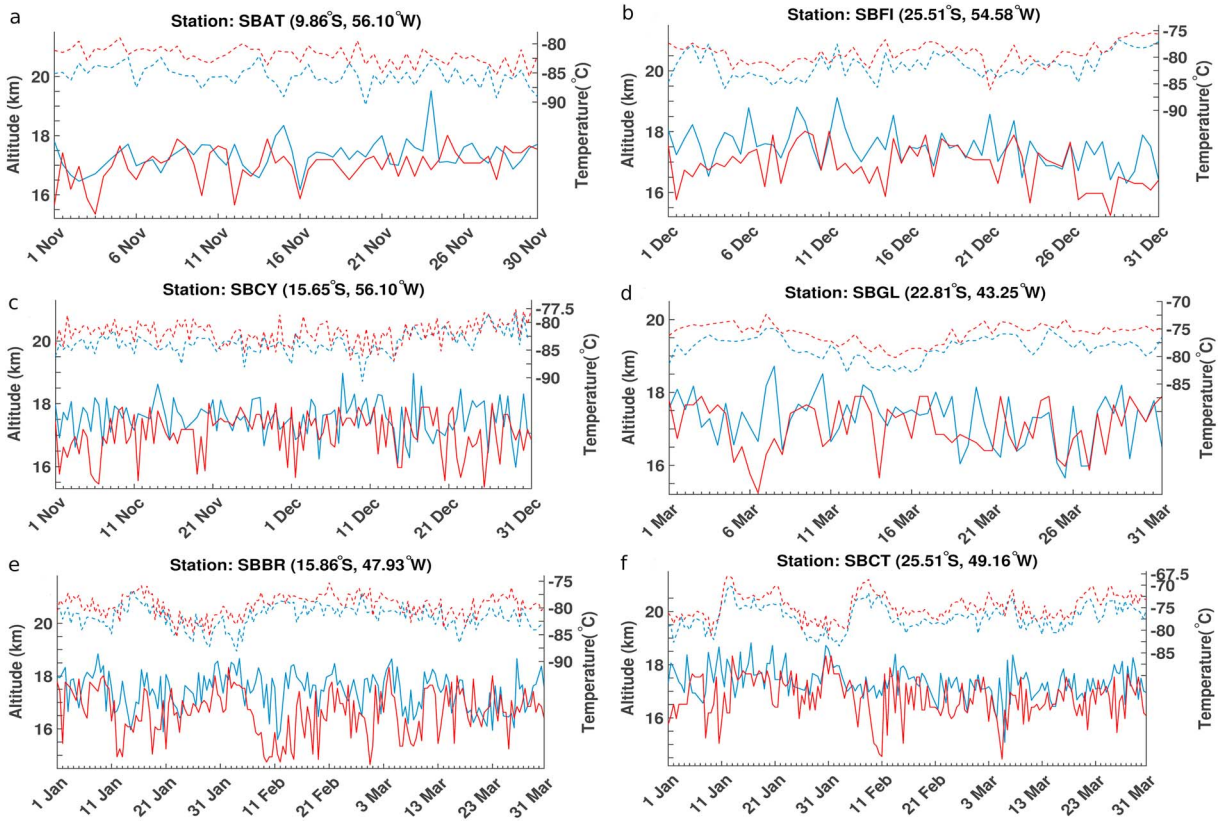

Figure 2. Cold-point tropopause depicting its altitude (solid lines; left *y* axis) and temperature (dotted lines; right *y* axis) as a function of time (different periods) from radiosonde measurements (blue) and the concurrent cold-point tropopause evolution generated by Brazilian version of Regional Atmospheric Modeling System (red) at different stations over Brazil: (a) SBAT during November 2012, (b) SBFI during December 2012, (c) SBCY during November–December 2012, (d) SBGL during March 2013, (e) SBBR during January–March 2013, and (f) SBCT during January–March 2013.

4.2. WV Mixing Ratio: TRO-Pico Campaign

Figure 3 shows a comparison of the balloon-borne WV measurements performed during the TRO-Pico campaign at Bauru with the WV profiles from the BRAMS. Most of the profiles shown in Figure 3 belong to the IOP2 (blue and red lines) and also include a few WV measurements obtained during November and December 2012 (black lines) and March 2013 (green lines), that is, part of the FMOP. Here the measurements are obtained from both the balloon-borne Pico-SLDA (solid lines) and FLASH-B (dotted lines) hygrometers. Maximum and minimum values of H_2O mixing ratio from the MLS: version 4.2 data are also shown for the same period (dots).

Figure 3a clearly highlights that the WV profiles are usually wetter at the beginning of the wet season (black lines) and drier at the end (green lines). The IOP2 measurements at the peak of the convective activity (blue and red profiles) depict a variability in between the beginning and the end of the wet season. However, the period at the end of January/beginning of February 2013 is observed to be very dry (red lines) with H_2O mixing ratio as low as ~2.0 ppmv in the hygropause. Referring to Figures 1 and 3, it can be concluded that the driest period in the TTL corresponds to the coldest period during the IOP2, suggesting dehydration associated with the cold temperature. This striking feature is in line with the observations reported by Evan et al. (2015) in the context of the 2013 ATTREX campaign (Jensen et al., 2013; Jensen, Pfister, et al., 2017). They report very dry measurements of WV from the Global Hawk Aircraft as low as 1.2 ppmv in the stratospheric part of the TTL over the Pacific Ocean on 26 February 2013. This noticeable feature happens later than the dry period during the IOP2 over Brazil. However, Evan et al. (2015) make the link between these dry and cold measurements with a SSW in the Arctic which started at the end of December 2012, and lasted until 23 January 2013. The consecutive TTL cooling was at a maximum around 23 January but was still cold until 1 February 2013 within the latitudes

Table 1
Biases in CPT Altitude (z) and Temperature (T)

Stations	$\sigma(\delta z)$ (km)	$\sigma(\delta T)$ (°C)	$\bar{X}_z$ (km)	$\bar{X}_T$ (°C)
SBAT	0.705	1.68	−0.319	3.445
SBCT	0.855	1.31	−0.600	2.407
SBFI	0.700	2.09	−0.589	2.188
SBBR	0.958	1.57	−0.803	2.068
SBCY	0.877	1.85	−0.441	1.828
SBGL	0.877	1.34	−0.216	2.613

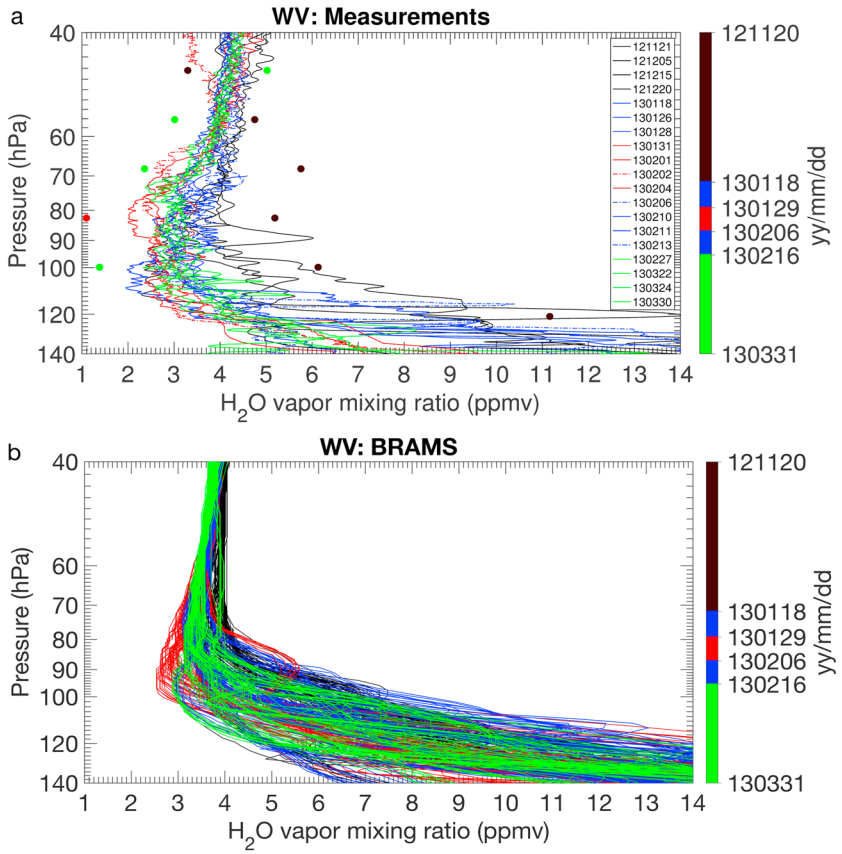

Figure 3. (a) Water vapor (WV) mixing ratio, measured by the Pico-SDLA (solid lines) and FLASH-B (dotted lines) H_2O spectrometers during the TRO-Pico campaign at Bauru. The minimum and maximum H_2O mixing ratios of corresponding pressure levels during the 5 months of observation period in the Bauru region are also shown (dots) from Microwave Limb Sounder: version 4.2 measurements for a domain of 24.00°S to 19.00°S and 55.50°W to 43.50°W. (b) WV profiles from the Brazilian version of Regional Atmospheric Modeling System (BRAMS) simulation at Bauru. Profiles for 1200 coordinated universal time to 2359 coordinated universal time are shown starting from 20 November 2012 to 30 March 2013 to be better comparable with the broad variability of WV profiles akin to deep convection from the hygrometer measurements.

ranging from 15.0°N to 15.0°S at the CPT and is compatible with the coldest period observed in Brazil around 1 February 2013 during TRO-Pico (Figure 1)—additional comments are also given in section S1 in the supporting information. More WV profiles are shown for the BRAMS in Figure 3b in order to have a broader view of the modeled WV variability during the FMOP.

In Figure 3, the time evolution of the wettest (black lines) and driest (red lines) periods, both in the measurements and in the simulation, is similar. It is also important to note that the driest (hygropause) profiles in the modeled TTL also correspond to the end of January/beginning of February 2013 with the mixing ratios decreasing to ~2.4 ppmv in the hygropause, which is close to the hygrometers measurements from the TRO-Pico, though not as dry; it is note worthy that on 31 January 2013, Pico-SDLA measurement is 2.0 ± 0.1 ppmv at this pressure level. It can be concluded that the WV variability in the region of Bauru, at least during the IOP2, was likely driven by large-scale processes rather than just local deep convection. This is consistent with the conclusion reached from the analysis in section 4.1. Maximum and minimum H_2O mixing ratios available for each pressure level during the FMOP for the MLS: version 4.2 measurements suggest such large-scale dehydration processes. BRAMS cannot fully succeed in computing quantitatively a TTL with very dry conditions in comparison to the observations. Several reasons can be suggested. First, the warmer conditions in the model lead to an underestimation of dehydration, which is concluded by using T_{sat} calculation as in Dessler et al. (1995)—see section S2 in the supporting information—and shows that a colder condition by ~2°C in the model could lead to a drier hygropause by ~0.4 ppmv, as obtained during the TRO-Pico campaign. Second, the ECMWF operational analyses used for nudging the grid points of the simulation

for initial and boundary conditions are themselves wetter than the observations, noting that the minimum value of H_2O mixing ratio in ECMWF at the hygropause at a location (22.00°S, 49.00°W) near Bauru is ~2.3 ppmv during the driest period of IOP2.

5. Cloud Tops in BRAMS

A set of different criteria are applied in BRAMS to assign cloud tops for thick deep convective clouds, shallow cumulus clouds, and cirrus clouds, so that the obtained cloudy column can be representative of SAFNWC products (space constraint restricts to show the sensitivity tests carried out to decide the cloud column using the ice + liquid mixing ratio). The condensed water content (ice + liquid, g kg^{-1}) is calculated for each level in the BRAMS model using three conditions following the decrease of condensed water with altitude in the different stages of development of convective clouds (Hong et al., 2004). First, if there is any vertical profile having a layer of the condensed water content concentration >0.3 g kg^{-1}, we choose the cloud top of the corresponding grid point to be the highest level having a concentration >0.15 g kg^{-1}. Otherwise, for profiles reaching a water content concentration >0.15 g kg^{-1}, we choose the cloud top to be the highest level having a water content concentration of >0.12 g kg^{-1}. Finally, if both conditions are not fulfilled, the altitude of the cloud top is chosen to be always the layer for which the water content of the corresponding grid point is >0.1 g kg^{-1} with the highest altitude.

5.1. GOES-12 Versus BRAMS

The estimated cloud tops in BRAMS, calculated every 3 h during the FMOP, viz., 0000, 0300, 0600, 0900, 1200, 1500, 1800, and 2100 coordinated universal time (UTC) are used for the 2-D cross-correlation (CC) analysis (two parameters: position and altitude of cloud tops) with the corresponding SAFNWC products (see Figure 4 for the whole FMOP and Figure 5 for example of direct cloud top comparisons). The satellite data are regridded to 20 km × 20 km resolution before comparing with the modeled cloud top. The CC formula is explained in Appendix A.

In Figure 4a, black areas indicate the absence of SAFNWC products, while white areas represent a null relation. This also corresponds to the situation where most of the grid points within the domain of simulation have no clouds at all, both in BRAMS and GOES-12, respectively. Most of the patterns show positive correlation (blue). The maximum agreement between GOES-12 and BRAMS is found to be 0.67, as can be seen from Figure 5a versus 5b, where the modeled cloud cells are at comparable position and altitude as observed by GOES-12, leading to a positive and high correlation coefficient. Concurrently, only very short periods during the FMOP depict negative correlation (brown), with the lowest value being −0.14. This is demonstrated in Figure 5c versus 5d, where the modeled cloud tops are found where there are no clouds in GOES-12. Thus, most of the time such cases explain the negative or low correlations obtained.

The best correlations are obtained for the period between 1800 UTC (1500 local time (LT)) and 0600 UTC (0300 LT). This corresponds to the period of most mature convection after 1500 LT, or the less active phase before 0300 LT. During the period 2100–2359 UTC, a large cloud cover is commonly observed, while during the rest of the night, a lesser cloud coverage is retrieved from BRAMS, as well as from GOES-12, yielding a good correlation. Similarly, the agreement is less good at the times when convection is starting to be trigged but has not yet reached its mature phase (early afternoon or later, viz., 0900–1500 UTC or 0600–1200 LT), which confirms the well known diurnal cycle of continental deep convection (Carminati et al., 2014; Khaykin et al., 2013; Liu & Zipser, 2005). The model may not be able to trigger this deep convection exactly at a given location at a correct time. But later in the afternoon during the more mature stage of deep convection, the model is performing better, as would be expected.

Figure 4b highlights BRAMS ability in simulating high clouds during the FMOP. It represents three time series illustrating the average value of the percentage of occurrence of high clouds (>10 km) calculated on a daily basis. Since we extract all types of optically thick clouds from GOES-12 (red line), the introduction of another parameter to observe only the deep convective cloud (dotted black line) makes it more specific in terms of the temporal trend to evaluate BRAMS. The chosen parameters are CTTH_Height and CTTH_Effect from the SAFNWC products, where CTTH_Height accounts mostly for all types of optically thick clouds, but the addition of a condition CTTH_Effect = 100 to the former parameter allows to discriminate only optically thick convective clouds (Derrien et al., 2013). Note that in the CC calculation (Figure 4a), only the CTTH_Height parameter is considered. Thus, it can be deduced that percentagewise, modeled high clouds are comparable with GOES-12

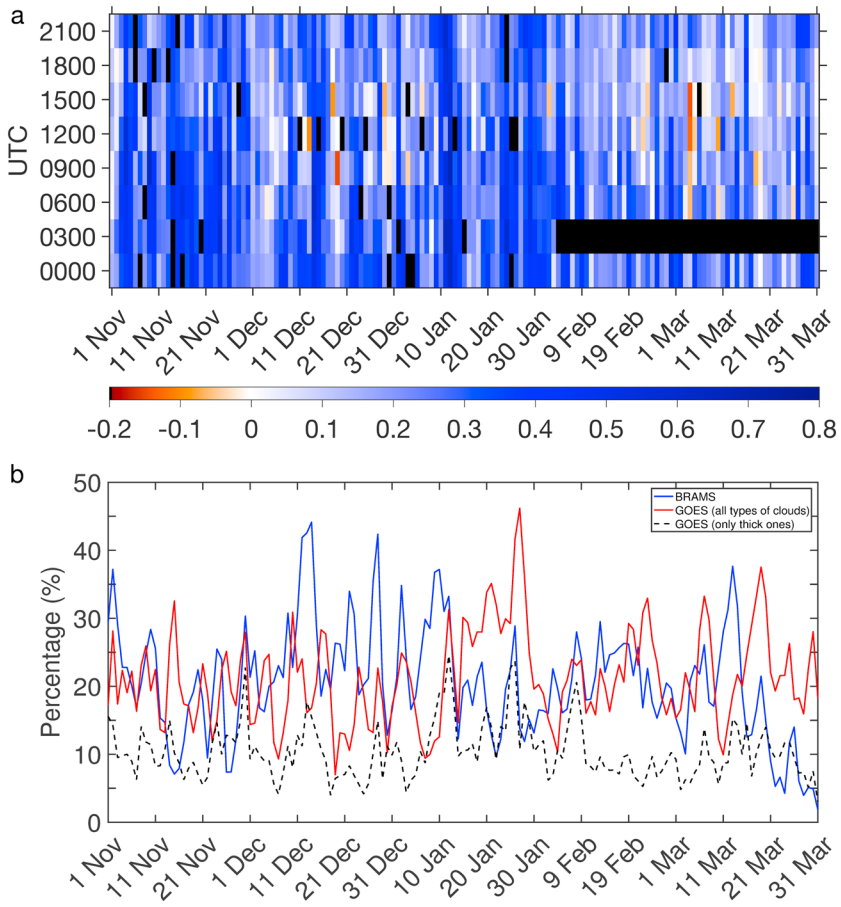

Figure 4. (a) Cross-correlation coefficients between the cloud tops measured by the Geostationary Operational Environmental Satellite (GOES)-12 satellite and calculated by the Brazilian version of Regional Atmospheric Modeling System (BRAMS) model for the full domain of simulation during the 5 months of observation period. The coefficients are calculated every 3 h starting from 1 November 2012 0000 coordinated universal time to 31 March 2013 2100 coordinated universal time. (b) Mean value of the percentage of cloud tops >10 km, calculated on a daily basis, for BRAMS (blue line) and GOES-12. The red line represents the high clouds in GOES-12 (including all types of optically thick clouds), while the black dotted line corresponds to only very thick convective clouds.

(blue versus red lines). In addition, the temporal trend of BRAMS (blue line) is typically coherent with GOES-12 (dotted black line), while considering only thick convective clouds in GOES-12. Therefore, the modeled and observed cloud tops are consistent.

5.2. MHS Versus BRAMS

Figures 6a and 6b depict the distribution of the modeled cloud altitude at and nearby the COV locations, respectively, detected by the satellite-borne MHS. Figure 6a shows an overall good ability of BRAMS to produce high cloud tops exactly at the position of overshooting cells detected by MHS. In order to account for possible errors in the modeled location of the high clouds, namely, if (x, y) denotes the COV location from MHS, then $(x + \delta x, y + \delta y)$ corresponds to the highest cloud top in the BRAMS model output, where $\delta x + \delta y$ are <50 km, Figure 6b should be considered. It confirms that the highest altitude of the cloud tops generated by BRAMS around a COV detected by MHS is usually very high (sometimes up to 16 km to 17 km for the maximum of the distribution, just below the 380 K isentrope in the simulation).

The main difference between Figure 6a versus 6b is the bell shape distribution of the altitude of cloud tops below the overshooting cells. The bell shape in Figure 6a starts at a lower altitude of 10 km than in the case of Figure 6b, which is 11 km. Furthermore, the maximum of high cloud distribution, that is, 19% for cloud tops from 13 km to 14 km, is lower for a low range of altitude than the maximum value obtained in the bell shape of Figure 6b, that is, 23% for a higher range of 14 km to 15 km. This implies that the highest modeled

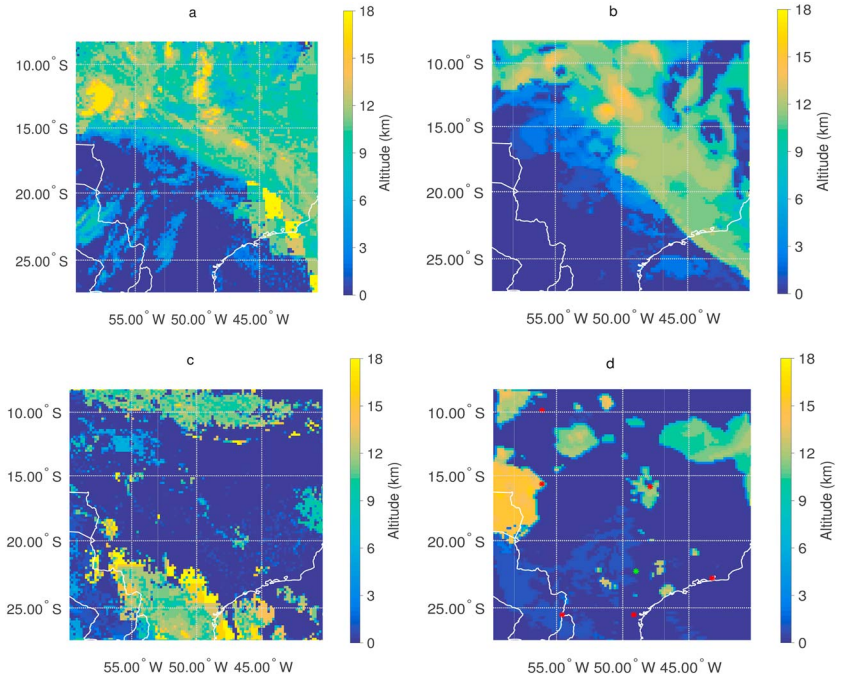

Figure 5. Cloud tops: (a) and (c) measured by the Geostationary Operational Environmental Satellite 12 satellite on 12 January 2013 0915 coordinated universal time and 4 March 4 2013 1515 coordinated universal time, respectively. (b) and (d) are from the Brazilian version of Regional Atmospheric Modeling System model during the same time period, as in (a) and (c), respectively. The locations of radio sounding stations from the upper-air database (red dots) and Bauru (green dot) are only shown in (d).

cloud tops around a COV location are spread in a limited range of high altitudes. In case of Figure 6b, the occurrence of high clouds (14 km to 17 km) is higher with respect to the case Figure 6a. The number of COV occurrence within the bell in Figure 6a, typically for cloud tops higher than 11 km, accounts for 63%, whereas in Figure 6b, it accounts for 75%. It can be concluded that accounting for a possible small error in the computed high cloud positions, the agreement improves significantly in the modeled high clouds versus MHS-detected overshooting cells. This analysis highlights the ability of BRAMS in positioning the highest cloud cells correctly.

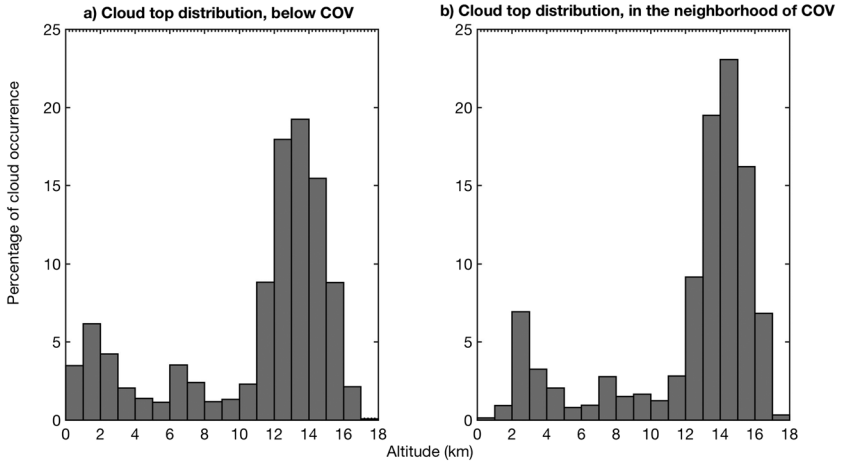

Figure 6. Histograms of the cloud top altitudes from Brazilian version of Regional Atmospheric Modeling System at the locations of overshooting cells (>14 km) detected by Microwave Humidity Sounder from 1 November 2012 to 31 March 2013 (5 months of observation period). (a) Cloud top altitude distribution exactly at the positions of overshooting cells; (b) distribution of the highest cloud tops present within the ~50 km radius of overshooting cells. COV = convective overshooting.

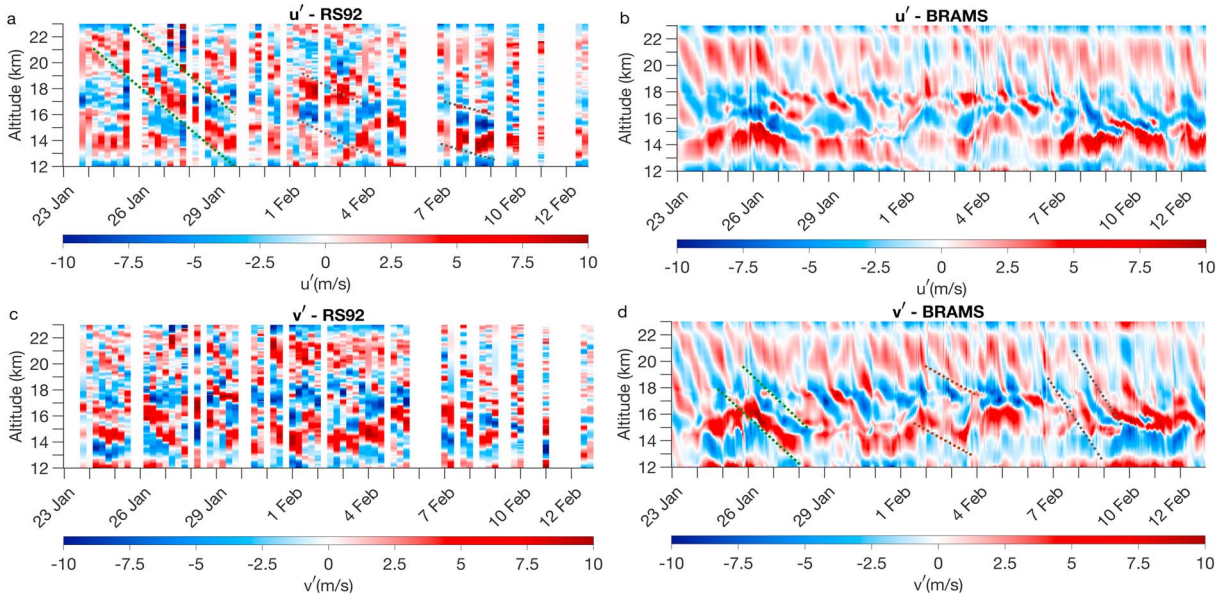

Figure 7. Perturbed wind profiles at Bauru from the RS92 measurements during the TRO-Pico campaign and from the Brazilian version of Regional Atmospheric Modeling System (BRAMS) model are shown for the period 23 January to 12 February 2013. (a) RS92 u' profile, (b) BRAMS u' profile, (c) RS92 v' profile, and (d) BRAMS v' profile. The blanks in the RS92 measurements correspond to the absence of data. Clearly visible gravity wave patterns are highlighted with dotted lines in (a) and (d).

6. Gravity Waves

Since it has been shown that gravity waves can influence the presence of cirrus ice particles in the TTL through the temperature field (e.g., Dinh et al., 2016; Schoeberl et al., 2016), it is worth investigating the ability of the model to reproduce the main wave patterns observed during to the TRO-Pico campaign, based on the RS92 measurements.

6.1. Horizontal Wind Perturbation Profiles

Tsuda et al. (1992) and Tsuda, Murayama, Wiryosumarto, et al. (1994) depict the detection of the inertia-gravity waves from the RS92 PTU RS. In this paper, the RS92 RS of the TRO-Pico campaign at Bauru are used to investigate the inertia-gravity waves during the IOP2. The zonal wind perturbation profile (u') is calculated by subtracting the third-order polynomial function fit of the u profile from itself (Hankinson et al., 2014; Tsuda, Murayama, Nakamura, et al., 1994); simultaneously, the same parameters are calculated from the simulation at Bauru. The polynomial function fit of the zonal wind profile is the mean wind profile ($\bar{u}$). Therefore, the wind profile can be expressed as $u(x, y, z, t) = \bar{u}(z, t) + u'(x, y, z, t)$. Similarly, the calculations are performed on the meridional wind (v).

Figure 7 depicts the vertical and temporal trends of the perturbed horizontal velocity from both the RS92 measurements and BRAMS simulations, respectively. In the velocity perturbations, the pattern of oscillations highlights the influence of inertia-gravity waves with a constant phase dispersing downward with time, typical of a negative vertical wave number and a positive horizontal wave number, respectively. The modeled profiles show about the same order of magnitude and patterns of oscillation, as in the measurements during 24–28 January and 2–3 and 7–9 February 2013, and are reasonably comparable with respect to the observed wavelength and periodicity of the inertia-gravity waves (Table 2). It is noticeable that, especially from u' (less from v', more noisy) around 28 January 2013, there is a wave period of about 1 day (more comments in section 6.2) with a vertical wavelength of ~3 km. In the BRAMS around 28 January 1200 UTC, we obtain the same order of magnitude of periodicity with a vertical wavelength of ~2.4 km. It is more visible on the modeled v' profiles than the corresponding u' profiles. Thus, it can be concluded that BRAMS is able to represent the typical behavior of the inertia-gravity waves in the TTL.

6.2. Hodograph Analysis

A hodograph analysis of the u' and v' can highlight a monochromatic behavior of the wave, if it exhibits an elliptical shape (Alexander & Vincent, 2000; Fovell et al., 1992). From the ratio of major axis to minor axis

Table 2
Comparison of the Wave Parameters Derived From Hodograph Analysis of the RS92 Measurements and the Simulation for 28 January and 8 February 2013

Cases: profiles	$\frac{a}{b}$	N_B (s^{-1})	λ_z (m)	$\bar{v}$ ($m\ s^{-1}$)	λ_h (km)	T (h)
2100 UTC 28/1/13: RS92	1.2800	0.0200	2,800	0.63	1264	25.8
1200 UTC 28/1/13: BRAMS	1.1624	0.0189	2,400	2.87	1389	23.2
2000 UTC 8/2/13: RS92	2.3709	0.0200	2,520	−11.05	398	40.8
0900 UTC 8/2/13: BRAMS	1.9872	0.0192	2,440	−3.61	457	30.4

Note. UTC = coordinated universal time; BRAMS = Brazilian version of Regional Atmospheric Modeling System.

of the ellipse in the hodograph, information about the wave field with the rotation direction varying with altitude and many intrinsic wave properties can be deduced (Alexander & Holton, 1997; Tsuda et al., 1990). Specific cases obtained from the RS92 measurements during IOP2 of the TRO-Pico campaign and from the BRAMS are shown in Figure S3 in the supporting information, where at least a partially elliptical feature can be identified, indicating monochromaticity of the wave. The intrinsic frequency $\hat{\omega}$, observed in a frame of reference moving with the ambient wind $(\bar{u}, \bar{v})$, can be calculated from the ratio of major to minor axes of the ellipse, which is equal to the ratio of $\hat{\omega}$ to the Coriolis parameter (f). When this ratio is of the order 1, the dispersion relationship is $\hat{\omega}^2 - f^2 = \frac{N_B^2 K_h^2}{m^2}$, where N_B is the Brunt-Väisälä frequency, K_h is the horizontal wave number, and $m = \frac{2\pi}{\lambda_z}$ (Fritts & Alexander, 2003).

Table 2 summarizes the periodicities (T) obtained from the hodograph analysis—calculations are given in section S3 in the supporting information. The few hours of time lag between the measurements and the simulation producing gravity wave patterns can be affiliated with the sporadic distribution of their sources, that is, the deep convection.

6.3. Influence of ECMWF on BRAMS

In section 4, it is shown that the nudging of ECMWF operational analyses at the boundary conditions could play a role in the temperature and WV variability in the BRAMS results. Therefore, it is important to evaluate its role in the modeled wave activity as well, especially for long waves that can propagate horizontally far from its source. It is found that in the ECMWF operational analyses used for nudging the simulation grid boundary condition and initialization, a similar oscillation is present in the u and v profiles, respectively, corresponding to the BRAMS ones. However, due to the poor vertical resolution of the ECMWF analyses, the vertical wavelength (λ_z) for the cases discussed in section 6.2 cannot be determined precisely. It could be roughly 6 km, but half of it ($\frac{\lambda_z}{2}$, as observed) could also be possible. The periodicity of the wave pattern in the south of the domain is ∼1 day. Thus, these numbers are compatible with the results from the simulation during the IOP2. Nevertheless, inside the domain, where the ECMWF analyses are not nudged, BRAMS is able to compute a wave pattern with higher harmonics corresponding to the observations, showing that either the source of the wave is inside the domain or that the physics inside BRAMS are able to better resolve this type of wave pattern.

7. Discussion of the Results and Future Objectives

The main objective of this paper is to evaluate the ability of the BRAMS model to capture correctly the key patterns of the tropical UTLS, which can have an impact on the stratospheric WV budget. In the current BRAMS setup, the deep and shallow convection is parameterized, and no SOC can be simulated. Having only deep convective activity, the model can simulate the temperature evolution with a relatively precise CPT variation throughout the FMOP at the Brazilian scale, albeit the modeled temperature near the TTL is warmer than the RS measurements. For the same reasons, the H_2O mixing ratio in BRAMS is observed to be slightly wetter than the measurements obtained from the TRO-Pico campaign. This can be partly attributed to BRAMS vertical resolution in the TTL, and also to the nudging with ECMWF operational analyses having a poor vertical resolution in the UTLS. The fact that no SOC can be simulated in the model may also play a role, as deep penetrating convection should cool down the TTL. Nevertheless, BRAMS follows a correct evolution of the thermal structure and WV abundance in the TTL. An important result also found is that the convective parameterization is exhibiting well the wide variability of convection in the TTL recorded in the observations, with a possible feedback of deep convection on the TTL's WV budget. Albeit the relatively coarser grid point resolution and larger-scale simulation, the model is able to reproduce relatively high cloud tops of 14 km to 17 km altitude

near the location of overshooting cells detected by MHS. Besides that, the spatial and temporal variability of modeled cloud cells are in good correlation with GOES-12. The BRAMS zonal and meridional winds show the presence of inertia-gravity waves, identified by the TRO-Pico radiosondes; this is also confirmed by the hodograph analysis of similar parameters (wavelength and periodicity).

In conclusion, the BRAMS mesoscale model appears to simulate adequately the main features of the tropical UTLS, emphasizing the notable role of temperature-driven processes in the tropopause to control the ingress of H_2O into the stratosphere. It can also be confirmed that SOC is of a smaller importance, yet possibly not negligible on a global scale, for the stratospheric WV budget. It is especially true for this particular wet season when the dramatic cooling and dehydration were observed above the Pacific, as well as in South America, as a response to a SSW in the Arctic.

A future objective will be the implementation of a subgrid-scale nudging for overshooting hydration (or dehydration) in the stratosphere with the same grid point resolution incorporating the MHS measurements, to explore the climatology of SOC on a continental scale.

Appendix A: Cross Correlation

The cross-correlation (CC) coefficients vary between −1 and 1, which quantifies the relationship (covariation) between two different sets of similar variables, and here the CC coefficients are obtained by the 2-D matrix multiplication method as employed by Kishtawal et al. (2009) for wider application, depicting the quality of modeled cloud cells with both intensity, spatial and temporal precision. Here CC is given by

$$\mathrm{CC} = \frac{\sum_m \sum_n (A_{mn} - \bar{A})(B_{mn} - \bar{B})}{\sqrt{\sum_m \sum_n (A_{mn} - \bar{A})^2 \sum_m \sum_n (B_{mn} - \bar{B})^2}}, \tag{A1}$$

where A and B are of the same dimensional matrices, and $\bar{A}$ and $\bar{B}$ are the mean values corresponding to the data from GOES-12 and BRAMS, respectively.

Acknowledgments
This work and the TRO-Pico project were supported by Agence Nationale de la Recherche (ANR) under contract ANR-2010-BLAN-609-01 and by the region Champagne-Ardenne in France. The Instituto de Pesquisas Meteorológicas (IPMet) and its staff are thanked for providing an infrastructure, manpower, and especially for their invaluable help with balloon operations during the TRO-Pico campaigns under a collaborative agreement with the French CNRS. TRO-Pico measurements were obtained through the ESPRI, a data center of the French Atmosphere Infrastructure AERIS (https://cds-espri.ipsl.upmc.fr/etherTypo/index.php?id=1691&L=1). This study was also sponsored by the Direction Générale de l'Armement (PRECIP-CLOUD project), Earth2observe project (funding from the European Union's Framework Program under grant agreement 603608), ANR-14-CE01-0014 MUSIC project, LEFE project "Overshoots à grande échelle," and the Centre National d'Études Spatiales (CNES). MHS data were obtained through the French Mixed Service Unit project ICARE/Climserv/AERIS. ICARE data and service center are acknowledged for providing GOES-12 and MHS satellite data (http://www.icare.univ-lille1.fr). The ECMWF is also acknowledged for granting access to their products (https://www.ecmwf.int/en/forecasts/datasets). Additionally, this project was also granted access to the HPC resources of CINES under the allocation of x2015015036 and x2016015036 made by GENCI (Grand Equipement National de Calcul Intensif) and was also allowed to the HPC resources of Centre de Calcul ROMEO under the project ID:669.

References

Alexander, M. J., & Holton, J. R. (1997). A model study of zonal forcing in the equatorial stratosphere by convectively induced gravity waves. *Journal of the Atmospheric Sciences*, *54*(3), 408–419.

Alexander, M. J., Holton, J. R., & Durran, D. R. (1995). The gravity wave response above deep convection in a squall line simulation. *Journal of the Atmospheric Sciences*, *52*(12), 2212–2226.

Alexander, M. J., & Vincent, R. A. (2000). Gravity waves in the tropical lower stratosphere: A model study of seasonal and interannual variability. *Journal of Geophysical Research*, *105*, 17,983–17,993.

Arteta, J., Marécal, V., & Rivière, E. D. (2009). Regional modelling of tracer transport by tropical convection — Part 1: Sensitivity to convection parameterization. *Atmospheric Chemistry and Physics*, *9*(18), 7081–7100.

Avery, M. A., Davis, S. M., Rosenlof, K. H., Ye, H., & Dessler, A. E. (2017). Large anomalies in lower stratospheric water vapour and ice during the 2015-2016 El Nino. *Nature Geoscience*, *10*(6), 405–409.

Bertaux, J.-L., & Delannoy, A. (1978). Premières measures stratosphériques par un hygromètre à fluorescence ultraviolette. *Comptes Rendus de l'Académie des Sciences*, *286*, 191–194.

Brewer, A. (1949). Evidence for a world circulation provided by the measurements of helium and water vapour distribution in the stratosphere. *Quarterly Journal of the Royal Meteorological Society*, *75*(326), 351–363.

Carminati, F., Ricaud, P., Pommereau, J.-P., Rivière, E., Khaykin, S., Attié, J.-L., & Warner, J. (2014). Impact of tropical land convection on the water vapour budget in the tropical tropopause layer. *Atmospheric Chemistry and Physics*, *14*(12), 6195–6211.

Chaboureau, J.-P., Cammas, J.-P., Duron, J., Mascart, P. J., Sitnikov, N. M., & Voessing, H.-J. (2007). A numerical study of tropical cross-tropopause transport by convective overshoots. *Atmospheric Chemistry and Physics*, *7*(7), 1731–1740.

Chemel, C., Russo, M. R., Pyle, J. A., Sokhi, R. S., & Schiller, C. (2009). Quantifying the imprint of a severe hector thunderstorm during ACTIVE/SCOUT-O3 onto the water content in the upper troposphere/lower stratosphere. *Monthly Weather Review*, *137*(8), 2493–2514.

Corti, T., Luo, B. P., de Reus, M., Brunner, D., Cairo, F., Mahoney, M. J., et al. (2008). Unprecedented evidence for deep convection hydrating the tropical stratosphere. *Geophysical Research Letters*, *35*, L10810. https://doi.org/10.1029/2008GL033641

Cotton, W. R., Pielke Sr. R. A., Walko, R. L., Liston, G. E., Tremback, C. J., Jiang, H., et al. (2003). RAMS 2001: Current status and future directions. *Meteorology and Atmospheric Physics*, *82*(1), 5–29.

Danielsen, E. F. (1982). A dehydration mechanism for the stratosphere. *Geophysical Research Letters*, *9*(6), 605–608.

Dauhut, T., Chaboureau, J.-P., Escobar, J., & Mascart, P. (2015). Large-eddy simulations of hector the convector making the stratosphere wetter. *Atmospheric Science Letters*, *16*(2), 135–140.

Derrien, M., Gléau, H., & Fernandez, P. (2013). Algorithm theoretical basis document for cloud products (CMA-PGE01 v3. 2, CT-PGE02 v2. 2, CTTH-PGE03 v2. 2) (Tech. Rep.). SAF/NWC/CDOP2/MFL/SCI/ATBD/01.

Derrien, M., & Gléau, H. L. (2005). MSG/SEVIRI cloud mask and type from SAFNWC. *International Journal of Remote Sensing*, *26*(21), 4707–4732.

Dessler, A. E., Hintsa, E. J., Weinstock, E. M., Anderson, J. G., & Chan, K. R. (1995). Mechanisms controlling water vapor in the lower stratosphere: "A tale of two stratospheres". *Journal of Geophysical Research*, *100*(D11), 23,167–23,172.

Dessler, A. E., Schoeberl, M. R., Wang, T., Davis, S. M., & Rosenlof, K. H. (2013). Stratospheric water vapor feedback. *Proceedings of the National Academy of Sciences*, *110*(45), 18,087–18,091.

Dessler, A. E., Schoeberl, M. R., Wang, T., Davis, S. M., Rosenlof, K. H., & Vernier, J.-P. (2014). Variations of stratospheric water vapor over the past three decades. *Journal of Geophysical Research: Atmospheres*, *119*, 12,588–12,598. https://doi.org/10.1002/2014JD021712

Dessler, A. E., Ye, H., Wang, T., Schoeberl, M., Oman, L., Douglass, A., et al. (2016). Transport of ice into the stratosphere and the humidification of the stratosphere over the 21st century. *Geophysical Research Letters*, *43*, 2323–2329. https://doi.org/10.1002/2016GL067991

Dinh, T., Podglajen, A., Hertzog, A., Legras, B., & Plougonven, R. (2016). Effect of gravity wave temperature fluctuations on homogeneous ice nucleation in the tropical tropopause layer. *Atmospheric Chemistry and Physics*, *16*(1), 35–46.

Evan, S., Rosenlof, K. H., Dudhia, J., Hassler, B., & Davis, S. M. (2013). The representation of the TTL in a tropical channel version of the WRF model. *Journal of Geophysical Research: Atmospheres*, *118*, 2835–2848. https://doi.org/10.1002/jgrd.50288

Evan, S., Rosenlof, K. H., Thornberry, T., Rollins, A., & Khaykin, S. (2015). TTL cooling and drying during the January 2013 stratospheric sudden warming. *Quarterly Journal of the Royal Meteorological Society*, *141*(693), 3030–3039.

Forster, P. M. d. F., & Shine, K. P. (1999). Stratospheric water vapour changes as a possible contributor to observed stratospheric cooling. *Geophysical Research Letters*, *26*(21), 3309–3312.

Fovell, R., Durran, D., & Holton, J. R. (1992). Numerical simulations of convectively generated stratospheric gravity waves. *Journal of the Atmospheric Sciences*, *49*(16), 1427–1442.

Freitas, S. R., Longo, K. M., Silva Dias, M. A. F., Chatfield, R., Silva Dias, P., Artaxo, P., et al. (2009). The Coupled Aerosol and Tracer Transport model to the Brazilian developments on the Regional Atmospheric Modeling System (CATT-BRAMS)—Part 1: Model description and evaluation. *Atmospheric Chemistry and Physics*, *9*(8), 2843–2861.

Fritts, D. C., & Alexander, M. J. (2003). Gravity wave dynamics and effects in the middle atmosphere. *Reviews of Geophysics*, *41*(1), 1003. https://doi.org/10.1029/2001RG000106

Fueglistaler, S., Dessler, A. E., Dunkerton, T. J., Folkins, I., Fu, Q., & Mote, P. W. (2009). Tropical tropopause layer. *Reviews of Geophysics*, *47*, RG1004. https://doi.org/10.1029/2008RG000267

Funatsu, B. M., Dubreuil, V., Claud, C., Arvor, D., & Gan, M. A. (2012). Convective activity in Mato Grosso state (Brazil) from microwave satellite observations: Comparisons between AMSU and TRMM data sets. *Journal of Geophysical Research*, *117*, D16109. https://doi.org/10.1029/2011JD017259

Garnier, A., Pelon, J., Dubuisson, P., Faivre, M., Chomette, O., Pascal, N., & Kratz, D. P. (2012). Retrieval of cloud properties using CALIPSO imaging infrared radiometer. Part I: Effective emissivity and optical depth. *Journal of Applied Meteorology and Climatology*, *51*(7), 1407–1425.

Gettelman, A., & de F Forster, P. M. (2002). A climatology of the tropical tropopause layer. *Journal of the Meteorological Society of Japan. Ser. II*, *80*(4B), 911–924.

Gettelman, A., Forster, P. M. d. F., Fujiwara, M., Fu, Q., Vömel, H., Gohar, L. K., et al. (2004). Radiation balance of the tropical tropopause layer. *Journal of Geophysical Research*, *109*, D07103. https://doi.org/10.1029/2003JD004190

Ghysels, M., Rivière, E. D., Khaykin, S., Stoeffler, C., Amarouche, N., Pommereau, J.-P., et al. (2016). Intercomparison of in situ water vapor balloon-borne measurements from Pico-SDLA H_2O and FLASH-B in the tropical UTLS. *Atmospheric Measurement Techniques*, *9*(3), 1207–1219.

Graf, H.-F., Kirchner, I., & Perlwitz, J. (1998). Changing lower stratospheric circulation: The role of ozone and greenhouse gases. *Journal of Geophysical Research*, *103*(D10), 11,251–11,261.

Grell, G. A., & Dévényi, D. (2002). A generalized approach to parameterizing convection combining ensemble and data assimilation techniques. *Geophysical Research Letters*, *29*(14), 1693. https://doi.org/10.1029/2002GL015311

Hankinson, M. C. N., Reeder, M. J., & Lane, T. P. (2014). Gravity waves generated by convection during TWP-ICE: I. Inertia-gravity waves. *Journal of Geophysical Research: Atmospheres*, *119*, 5269–5282. https://doi.org/10.1002/2013JD020724

Harrington, J. Y. (1997). The effects of radiative and microphysical processes on simulated warm and transition season Arctic stratus (PhD thesis). Fort Collins: Colorado State University.

Hasebe, F., Fujiwara, M., Nishi, N., Shiotani, M., Vömel, H., Oltmans, S., et al. (2007). In situ observations of dehydrated air parcels advected horizontally in the tropical tropopause layer of the western Pacific. *Atmospheric Chemistry and Physics*, *7*(3), 803–813.

Hassim, M. E. E., & Lane, T. P. (2010). A model study on the influence of overshooting convection on TTL water vapour. *Atmospheric Chemistry and Physics*, *10*(20), 9833–9849.

Highwood, E. J., & Hoskins, B. J. (1998). The tropical tropopause. *Quarterly Journal of the Royal Meteorological Society*, *124*(549), 1579–1604.

Holton, J. R. (1983). The influence of gravity wave breaking on the general circulation of the middle atmosphere. *Journal of the Atmospheric Sciences*, *40*(10), 2497–2507.

Holton, J. R., & Gettelman, A. (2001). Horizontal transport and the dehydration of the stratosphere. *Geophysical Research Letters*, *28*(14), 2799–2802.

Holton, J. R., Haynes, P. H., McIntyre, M. E., Douglass, A. R., Rood, R. B., & Pfister, L. (1995). Stratosphere-troposphere exchange. *Reviews of Geophysics*, *33*(4), 403–439.

Hong, G., Heygster, G., Miao, J., & Kunzi, K. (2005). Detection of tropical deep convective clouds from AMSU-B water vapor channels measurements. *Journal of Geophysical Research*, *110*, D05205. https://doi.org/10.1029/2004JD004949

Hong, G., Heygster, G., Notholt, J., & Buehler, S. A. (2008). Interannual to diurnal variations in tropical and subtropical deep convective clouds and convective overshooting from seven years of AMSU-B measurements. *Journal of Climate*, *21*(17), 4168–4189.

Hong, S.-Y., Dudhia, J., & Chen, S.-H. (2004). A revised approach to ice microphysical processes for the bulk parameterization of clouds and precipitation. *Monthly Weather Review*, *132*(1), 103–120.

Iwasaki, S., Shibata, T., Nakamoto, J., Okamoto, H., Ishimoto, H., & Kubota, H. (2010). Characteristics of deep convection measured by using the A-train constellation. *Journal of Geophysical Research*, *115*, D06207. https://doi.org/10.1029/2009JD013000

Jensen, E. J., Pfister, L., Jordan, D. E., Bui, T. V., Ueyama, R., Singh, H. B., et al. (2017). The NASA Airborne Tropical Tropopause Experiment: High-altitude aircraft measurements in the tropical western Pacific. *Bulletin of the American Meteorological Society*, *98*(1), 129–143.

Jensen, E. J., Pfister, L., Jordan, D. E., Fahey, D. W., Newman, P. A., Thornberry, T., et al. (2013). The NASA Airborne Tropical TRopopause EXperiment (ATTREX). *SPARC Newsletter*, *41*, 15–24.

Jensen, E. J., Thornberry, T. D., Rollins, A. W., Ueyama, R., Pfister, L., Bui, T., et al. (2017). Physical processes controlling the spatial distributions of relative humidity in the tropical tropopause layer over the Pacific. *Journal of Geophysical Research: Atmospheres*, *122*, 6094–6107. https://doi.org/10.1002/2017JD026632

Jewtoukoff, V., Plougonven, R., & Hertzog, A. (2013). Gravity waves generated by deep tropical convection: Estimates from balloon observations and mesoscale simulations. *Journal of Geophysical Research: Atmospheres*, *118*, 9690–9707. https://doi.org/10.1002/jgrd.50781

Khaykin, S., Pommereau, J.-P., Korshunov, L., Yushkov, V., Nielsen, J., Larsen, N., et al. (2009). Hydration of the lower stratosphere by ice crystal geysers over land convective systems. *Atmospheric Chemistry and Physics*, *9*(6), 2275–2287.

Khaykin, S. M., Pommereau, J.-P., & Hauchecorne, A. (2013). Impact of land convection on temperature diurnal variation in the tropical lower stratosphere inferred from COSMIC GPS radio occultations. *Atmospheric Chemistry and Physics*, *13*(13), 6391–6402.

Khaykin, S. M., Pommereau, J.-P., Riviere, E. D., Held, G., Ploeger, F., Ghysels, M., et al. (2016). Evidence of horizontal and vertical transport of water in the southern hemisphere tropical tropopause layer (TTL) from high-resolution balloon observations. *Atmospheric Chemistry and Physics*, *16*(18), 12,273–12,286.

Kim, J.-E., & Alexander, M. J. (2013). A new wave scheme for trajectory simulations of stratospheric water vapor. *Geophysical Research Letters*, *40*, 5286–5290. https://doi.org/10.1002/grl.50963

Kim, J.-E., & Alexander, M. J. (2015). Direct impacts of waves on tropical cold point tropopause temperature. *Geophysical Research Letters*, *42*, 1584–1592. https://doi.org/10.1002/2014GL062737

Kim, J.-E., Alexander, M. J., Bui, T. P., Dean-Day, J. M., Lawson, R. P., Woods, S., et al. (2016). Ubiquitous influence of waves on tropical high cirrus clouds. *Geophysical Research Letters*, *43*, 5895–5901. https://doi.org/10.1002/2016GL069293

Kirk-Davidoff, D. B., Hintsa, E. J., Anderson, J. G., & Keith, D. W. (1999). The effect of climate change on ozone depletion through changes in stratospheric water vapour. *Nature*, *402*(6760), 399–401.

Kishtawal, C. M., Deb, S. K., Pal, P. K., & Joshi, P. C. (2009). Estimation of atmospheric motion vectors from Kalpana-1 Imagers. *Journal of Applied Meteorology and Climatology*, *48*(11), 2410–2421.

Kuang, Z., & Bretherton, C. S. (2004). Convective influence on the heat balance of the tropical tropopause layer: A cloud-resolving model study. *Journal of the Atmospheric Sciences*, *61*(23), 2919–2927.

Küpper, C., Thuburn, J., Craig, G. C., & Birner, T. (2004). Mass and water transport into the tropical stratosphere: A cloud-resolving simulation. *Journal of Geophysical Research*, *109*, D10111. https://doi.org/10.1029/2004JD004541

Lelieveld, J., Brühl, C., Jöckel, P., Steil, B., Crutzen, P., Fischer, H., et al. (2007). Stratospheric dryness: Model simulations and satellite observations. *Atmospheric Chemistry and Physics*, *7*, 1313–1332.

Liu, C., & Zipser, E. J. (2005). Global distribution of convection penetrating the tropical tropopause. *Journal of Geophysical Research*, *110*, D23104. https://doi.org/10.1029/2005JD006063

Liu, X. M., Rivière, E. D., Marécal, V., Durry, G., Hamdouni, A., Arteta, J., & Khaykin, S. (2010). Stratospheric water vapour budget and convection overshooting the tropopause: Modelling study from SCOUT-AMMA. *Atmospheric Chemistry and Physics*, *10*(17), 8267–8286.

Liu, Y. S., Fueglistaler, S., & Haynes, P. H. (2010). Advection-condensation paradigm for stratospheric water vapor. *Journal of Geophysical Research*, *115*, D24307. https://doi.org/10.1029/2010JD014352

Livesey, N. J., Read, W. G., Wagner, P. A., Froidevaux, L., Lambert, A., Manney, G. L., et al. (2015). Version 4.2x level 2 data quality and description document (Tech. Rep. JPL D-33509). NASA Jet Propulsion Laboratory. version 4.2x-1.0.

Marécal, V., Durry, G., Longo, K., Freitas, S., Rivière, E. D., & Pirre, M. (2007). Mesoscale modelling of water vapour in the tropical UTLS: Two case studies from the HIBISCUS campaign. *Atmospheric Chemistry and Physics*, *7*(5), 1471–1489.

Menzel, W. P., Smith, W. L., & Stewart, T. R. (1983). Improved cloud motion wind vector and altitude assignment using VAS. *Journal of Climate and Applied Meteorology*, *22*(3), 377–384.

Meyers, M. P., Walko, R. L., Harrington, J. Y., & Cotton, W. R. (1997). New RAMS cloud microphysics parameterization. Part II: The two-moment scheme. *Atmospheric Research*, *45*(1), 3–39.

Minnis, P., Yost, C. R., Sun-Mack, S., & Chen, Y. (2008). Estimating the top altitude of optically thick ice clouds from thermal infrared satellite observations using CALIPSO data. *Geophysical Research Letters*, *35*, L12801. https://doi.org/10.1029/2008GL033947

Morrison, H., Thompson, G., & Tatarskii, V. (2009). Impact of cloud microphysics on the development of trailing stratiform precipitation in a simulated squall line: Comparison of one- and two-moment schemes. *Monthly Weather Review*, *137*(3), 991–1007.

Pielke, R. A., Cotton, W. R., Walko, R. L., Tremback, C. J., Lyons, W. A., Grasso, L. D., et al. (1992). A comprehensive meteorological modeling system—RAMS. *Meteorology and Atmospheric Physics*, *49*(1), 69–91.

Ramaswamy, V., Schwarzkopf, M., & Randel, W. (1996). Fingerprint of ozone depletion in the spatial and temporal pattern of recent lower-stratospheric cooling. *Nature*, *382*(6592), 616–618.

Randel, W. J., & Jensen, E. J. (2013). Physical processes in the tropical tropopause layer and their roles in a changing climate. *Nature Geoscience*, *6*(3), 169–176.

Randel, W. J., Wu, F., Vomel, H., Nedoluha, G. E., & Forster, P. (2006). Decreases in stratospheric water vapor after 2001: Links to changes in the tropical tropopause and the Brewer-Dobson circulation. *Journal of Geophysical Research*, *111*, D12312. https://doi.org/10.1029/2005JD006744

Romps, D. M., & Kuang, Z. (2009). Overshooting convection in tropical cyclones. *Geophysical Research Letters*, *36*, L09804. https://doi.org/10.1029/2009GL037396

Rysman, J.-F., Claud, C., Chaboureau, J.-P., Delanoë, J., & Funatsu, B. M. (2016). Severe convection in the mediterranean from microwave observations and a convection-permitting model. *Quarterly Journal of the Royal Meteorological Society*, *142*, 43–55.

Rysman, J.-F., Claud, C., & Delanoë, J. (2017). Monitoring deep convection and convective overshooting from 60°S to 60°N using MHS: A Cloudsat/CALIPSO-based assessment. *IEEE Geoscience and Remote Sensing Letters*, *14*(2), 159–163.

Schiller, C., Grooß, J.-U., Konopka, P., Plöger, F., Silva dos Santos, F. H., & Spelten, N. (2009). Hydration and dehydration at the tropical tropopause. *Atmospheric Chemistry and Physics*, *9*(24), 9647–9660.

Schmetz, J., Holmlund, K., Hoffman, J., Strauss, B., Mason, B., Gaertner, V., et al. (1993). Operational cloud-motion winds from Meteosat infrared images. *Journal of Applied Meteorology*, *32*(7), 1206–1225.

Schoeberl, M., Dessler, A., Ye, H., Wang, T., Avery, M., & Jensen, E. (2016). The impact of gravity waves and cloud nucleation threshold on stratospheric water and tropical tropospheric cloud fraction. *Earth and Space Science*, *3*, 295–305. https://doi.org/10.1002/2016EA000180

Schoeberl, M. R., & Dessler, A. E. (2011). Dehydration of the stratosphere. *Atmospheric Chemistry and Physics*, *11*(16), 8433–8446.

Schoeberl, M. R., Dessler, A. E., & Wang, T. (2012). Simulation of stratospheric water vapor and trends using three reanalyses. *Atmospheric Chemistry and Physics*, *12*(14), 6475–6487.

Schoeberl, M. R., Jensen, E. J., & Woods, S. (2015). Gravity waves amplify upper tropospheric dehydration by clouds. *Earth and Space Science*, *2*, 485–500. https://doi.org/10.1002/2015EA000127

Seidel, D. J., Ross, R. J., Angell, J. K., & Reid, G. C. (2001). Climatological characteristics of the tropical tropopause as revealed by radiosondes. *Journal of Geophysical Research*, *106*(D8), 7857–7878.

Sellers, P., Randall, D., Collatz, G., Berry, J., Field, C., Dazlich, D., et al. (1996). A revised land surface parameterization (SiB2) for atmospheric GCMs. Part I: Model formulation. *Journal of climate*, *9*(4), 676–705.

Sellers, P. J., Tucker, C. J., Collatz, G. J., Los, S. O., Justice, C. O., Dazlich, D. A., & Randall, D. A. (1996). A revised land surface parameterization (SiB2) for atmospheric GCMs. Part II: The generation of global fields of terrestrial biophysical parameters from satellite data. *Journal of Climate*, *9*(4), 706–737.

Shindell, D. T. (2001). Climate and ozone response to increased stratospheric water vapor. *Geophysical Research Letters*, *28*(8), 1551–1554.

Skamarock, W. C., Klemp, J. B., Dudhia, J., Gill, D. O., Barker, D. M., Wang, W., & Powers, J. G. (2005). A description of the advanced research WRF version 2 (Tech. Rep.) Boulder, CO: National Center For Atmospheric Research. Mesoscale and Microscale Meteorology Div.

Smalley, K. M., Dessler, A. E., Bekki, S., Deushi, M., Marchand, M., Morgenstern, O., et al. (2017). Contribution of different processes to changes in tropical lower-stratospheric water vapor in chemistry–climate models. *Atmospheric Chemistry and Physics*, *17*(13), 8031–8044.

Solomon, S. (1988). The mystery of the antarctic ozone "hole". *Reviews of Geophysics*, *26*(1), 131–148.

Solomon, S. (1999). Stratospheric ozone depletion: A review of concepts and history. *Reviews of Geophysics*, *37*(3), 275–316.

Solomon, S., Rosenlof, K. H., Portmann, R. W., Daniel, J. S., Davis, S. M., Sanford, T. J., & Plattner, G.-K. (2010). Contributions of stratospheric water vapor to decadal changes in the rate of global warming. *Science*, *327*(5970), 1219–1223.

Sèze, G., Pelon, J., Derrien, M., Le Gléau, H., & Six, B. (2015). Evaluation against CALIPSO lidar observations of the multi-geostationary cloud cover and type dataset assembled in the framework of the Megha-Tropiques mission. *Quarterly Journal of the Royal Meteorological Society*, *141*(688), 774–797.

Toon, O. B., Turco, R. P., Jordan, J., Goodman, J., & Ferry, G. (1989). Physical processes in polar stratospheric ice clouds. *Journal of Geophysical Research*, *94*(D9), 11,359–11,380.

Tsuda, T., Kato, S., Yokoi, T., Inoue, T., Yamamoto, M., VanZandt, T. E., et al. (1990). Gravity waves in the mesosphere observed with the middle and upper atmosphere radar. *Radio Science*, *25*(5), 1005–1018.

Tsuda, T., Murayama, Y., Oyama, K.-I., Schmidlin, F., Bittner, M., Kanzawa, H., et al. (1992). Rocketsonde observations of the middle atmosphere dynamics at Uchinoura (31°N, 131°E) during the DYANA campaign. Part II: Characteristics of gravity waves. *Journal of Geomagnetism and Geoelectricity*, *44*(11), 1009–1023.

Tsuda, T., Murayama, Y., Nakamura, T., Vincent, R., Manson, A., Meek, C., & Wilson, R. (1994). Variations of the gravity wave characteristics with height, season and latitude revealed by comparative observations. *Journal of Atmospheric and Terrestrial Physics*, *56*(5), 555–568.

Tsuda, T., Murayama, Y., Wiryosumarto, H., Harijono, S. W. B., & Kato, S. (1994). Radiosonde observations of equatorial atmosphere dynamics over Indonesia: 2. Characteristics of gravity waves. *Journal of Geophysical Research*, *99*(D5), 10,507–10,516.

Ueyama, R., Jensen, E. J., Pfister, L., & Kim, J.-E. (2015). Dynamical, convective, and microphysical control on wintertime distributions of water vapor and clouds in the tropical tropopause layer. *Journal of Geophysical Research: Atmospheres*, *120*, 10,483–10,500. https://doi.org/10.1002/2015JD023318

Vömel, H., Yushkov, V., Khaykin, S., Korshunov, L., Kyrö, E., & Kivi, R. (2007). Intercomparisons of stratospheric water vapor sensors: FLASH-B and NOAA/CMDL frost-point hygrometer. *Journal of Atmospheric and Oceanic Technology*, *24*(6), 941–952.

Wang, T., Dessler, A. E., Schoeberl, M. R., Randel, W. J., & Kim, J.-E. (2015). The impact of temperature vertical structure on trajectory modeling of stratospheric water vapor. *Atmospheric Chemistry and Physics*, *15*(6), 3517–3526.

Yan, X., Wright, J. S., Zheng, X., Livesey, N. J., Vömel, H., & Zhou, X. (2016). Validation of Aura MLS retrievals of temperature, water vapour and ozone in the upper troposphere and lower–middle stratosphere over the Tibetan Plateau during boreal summer. *Atmospheric Measurement Techniques*, *9*(8), 3547–3566.

Yushkov, V., Valery, A., & Serafim, M. (1998). Optical balloon hygrometer for upper troposphere and stratosphere water vapor measurements, *Optical remote sensing of the atmosphere and clouds* (Vol. 3501, 439 pp.). Beijing, China.